PHYSICS

Giant nonlinear optical wave mixing in a van der Waals correlated insulator

Li Yue[1,2]*†, Chang Liu[1]†, Shanshan Han[2,3], Hao Hong[4], Yijun Wang[4], Qiaomei Liu[1], Jiajie Qi[4], Yuan Li[1,5], Dong Wu[2], Kaihui Liu[4], Enge Wang[1,5], Tao Dong[1]*, Nanlin Wang[1,2,5]*

Optical nonlinearities are one of the most fascinating properties of two-dimensional (2D) materials. While tremendous efforts have been made to find and optimize the second-order optical nonlinearity in enormous 2D materials, opportunities to explore higher-order ones are elusive because of the much lower efficiency. Here, we report the giant high odd-order optical nonlinearities in centrosymmetric correlated van der Waals insulator manganese phosphorus triselenide. When illuminated by two near-infrared femtosecond lasers, the sample generates a series of profound four- and six-wave mixing outputs. The near-infrared third-order nonlinear susceptibility reaches near the highest record values of 2D materials. Comparative measurements to other prototypical nonlinear optical materials [lithium niobate, gallium(II) selenide, and tungsten disulfide] reveal its extraordinary wave mixing efficiency. The wave mixing processes are further used for nonlinear optical waveguide with multicolor emission. Our work highlights the promising prospect for future research of the nonlinear light-matter interactions in the correlated 2D system and for potential nonlinear photonic applications.

INTRODUCTION

The coherent nonlinear interaction between light and matter gives rise to intriguing nonlinear optical wave mixing phenomena (*1*, *2*), such as high harmonic generation (HHG), sum frequency generation (SFG), and four-wave mixing (FWM). Over the past decades, nonlinear optical wave mixing has played a crucial role in laser generation and manipulation, photon detection, and optical sensing (*1*–*6*). Nowadays, nonlinear optical wave mixing has become increasingly important in emerging fields such as quantum photonics, quantum information, and on-chip nanophotonics (*6*–*8*). As nonlinear optical responses are inherently weak, materials with large nonlinear susceptibility are essential. Traditional nonlinear optical materials are typically conventional bulk nonlinear crystals (e.g., beta barium borate and lithium niobate). They are limited by insufficiently large susceptibility, weak availability for nanointegration, and on-chip design due to the three dimensional covalent bonding (*1*, *5*, *6*) and therefore cannot satisfy the demands of next-generation nonlinear photonic research. Conversely, two-dimensional (2D) materials with van der Waals (vdW) structure advantageous for nanofabrication and bond-free integration (*9*) open up opportunities for application. In recent years, large nonlinear susceptibilities have been found in a variety of 2D materials such as graphene and transition metal dichalcogenides (*6*, *10*), which triggered tremendous research of the nonlinear optical properties of 2D materials and fabrication of advanced nanophotonic devices.

Despite tremendous research of the nonlinear optical properties of 2D materials, further exploration should be extended in several aspects. First, current studies mostly focus on the second-order nonlinear processes in noncentrosymmetic materials. The higher odd-order nonlinear processes, which, in principle, are independent of inversion symmetry and thus more versatile, are paid less attention since they are generally much less efficient than second-order process. In some cases, third-order nonlinear response is still achieved via cascaded second-order processes (*11*, *12*). As for the well-studied one with large odd-order susceptibilities (i.e., graphene), the conversion efficiency is highly restricted by the intense absorption with increasing thickness (*13*, *14*). Second, the widely studied second harmonic generation (SHG) and HHG are degenerate wave mixing processes under monochromatic laser excitation. Nondegenerate wave mixing processes (e.g., nondegenerate FWM), which require excitation by multiple wavelengths, are seldom studied. However, they have unique importance. The nondegeneracy provides different excitation quantum pathways for nonlinear light-matter interactions (*15*, *16*). The tunable time delay between different laser pulses enables tracking the temporal dynamics of the interacting system (*16*). Third, typical 2D nonlinear optical materials are simple systems with weak correlation effects and disentangled degrees of freedom. How the fancier physics, such as the electronic correlations and interacting subsystems, could affect the nonlinear light-matter interactions and modify the nonlinear optical responses remains elusive. To reach a deeper understanding in this field, one needs an ideal 2D system simultaneously hosting large optical nonlinearities, correlated degrees of freedom, and many-body effects.

In this work, our discovery of giant high-order nonlinear optical wave mixing in $MnPSe_3$ offers a great testground for the above questions. Transition metal phosphorous trichalcogenides MPX_3 (M = Mn, Ni, Fe, and Co; X = S and Se) are a family of 2D vdW correlated antiferromagnetic (AFM) insulators. In recent years, this family attracted intense interest for the rich correlations between charge, spin, and lattice subsystems (*17*–*20*), excitonic many-body quantum states (*20*–*22*), and tunable magnetic and optical properties (*21*, *23*–*25*). So far, plenty of studies have reported their unique optical properties [e.g., photoluminescence (*19*–*21*) and giant linear

[1]International Center for Quantum Materials, School of Physics, Peking University, Beijing 100871, China. [2]Beijing Academy of Quantum Information Sciences, Beijing 100193, China. [3]School of Materials Science and Engineering, Smart Sensing Interdisciplinary Science Center, Collaborative Innovation Center ofChemical Science and Engineering, Nankai University, Tianjin 300350, China. [4]State Key Laboratory for Mesoscopic Physics, Frontiers Science Center for Nano-optoelectronics, School of Physics, Peking University, Beijing 100871, China. [5]Collaborative Innovation Center of Quantum Matter, Beijing, China.
*Corresponding author. Email: lilyyue@pku.edu.cn (L.Y.); taodong@pku.edu.cn (T.D.); nlwang@pku.edu.cn (N.W.)
†These authors contributed equally to this work.

dichroism (*21*, *25*, *26*)] in fascinating association with the multiway interacting subsystems. In particular, the researches of the nonlinear optical responses in this family are limited to SHG in the low-temperature AFM phase with broken inversion symmetry (*23*, *27*–*29*).

In this work, we report the discovery of profound higher odd-order optical nonlinearities of this family at room temperature. When the $MnPSe_3$ (and $MnPS_3$, $NiPS_3$) samples are excited by two femtosecond lasers at 847 and 1280 nm, they generate profound nonlinear wave mixing outputs ranging from ultraviolet to visible wavelengths, including third harmonic generation (THG), nondegenerate four-wave mixing, and six-wave mixing.

RESULTS

We used several $MnPSe_3$ samples: an exfoliated bulk of ~20 μm in thickness glued onto a hollow copper platform to avoid using substrates and two thin films with thickness of ~1 μm and ~100 nm exfoliated on fused silica. Our experiment was performed at room temperature. Two near-infrared femtosecond lasers at 847 nm (power $P_1 = 5$ mW) and 1280 nm (power $P_2 = 10$ mW), with 50-kHz repetition rate, are focused onto a spot about 100 μm in diameter on the sample in noncollinear geometry by two lenses (see Materials and Methods and fig. S1). The peak intensities are ~0.03 TW/cm^2 for 847-nm laser and 0.06 TW/cm^2 for 1280-nm laser. The two excitation wavelengths are within the optical gap of $MnPSe_3$ and weakly absorbed (Fig. 1A). The optical gap of $MnPSe_3$ is reported at near 2.5 eV (*30*). At lower energies, there are in-gap excitations including d-d transition (~1.83 eV) and charge transfer transition (~2.27 eV) (*31*), which should be related to the fine features in Fig. 1A.

Figure 1B demonstrates the transmitted beams through the ~20-μm bulk sample directly viewed on a paper card. When the 847- and 1280-nm pulses are temporally separated, only two outgoing beams are seen (speckles B and E in Fig. 1B). While E is a direct view of the 847-nm laser, the visible beam B contains the THG of the 1280-nm laser. When the two impinging pulses are temporally overlapped, the sample emits new outgoing beams (speckles A, C, D, F, and G in Fig. 1B) arising from nondegenerate nonlinear wave mixing processes.

The nonlinear wave mixing process, $E_{new} \propto \chi^{(m)} E_1^{|m_1|} E_2^{|m_2|}$, generates new outgoing photons satisfying energy conservation $\omega_{new} = m_1\omega_1 + m_2\omega_2$ (Fig. 1D). Here, E_1 (E_2) and ω_1 (ω_2) refer to the electric field and photon energy of the 847-nm (1280-nm) laser. $\chi^{(m)}$ is the mth-order nonlinear susceptibility, with $m = |m_1| + |m_2|$ being odd integer due to inversion symmetry. In noncollinear geometry, new photons with momentum in the direction between the two excitation beams should be from all-sum processes (region II in Fig. 1, B and D), and photons emitted in the outside region should involve a difference process (regions I and III in Fig. 1, B and D). We measured the spectrum of each outgoing beam with other beams blocked using a NOVA high sensitive spectrometer, Ideaoptics, China (Fig. 1C). The measurements cover 300- to 980-nm wavelength range. The peaks are identified as all four-wave and six-wave mixing outputs within 300 to 980 nm as listed in Table 1. In particular, the spectrum at speckle G exhibits a second peak g′ centered at 723 nm (1.72 eV), matching none of the four-wave and six-wave mixing energies.

We studied the intensity of wave mixing peaks as a function of the excitation powers (Fig. 2). The power-law fit of data at low excitation powers gives power exponents consistent with expected $|m_1|$ and $|m_2|$ values, albeit slightly lower. At high excitation powers, most of the intensities, except for the P_2 dependence of signals a to c, start to deviate below the power-law fit and show saturation feature, as visualized

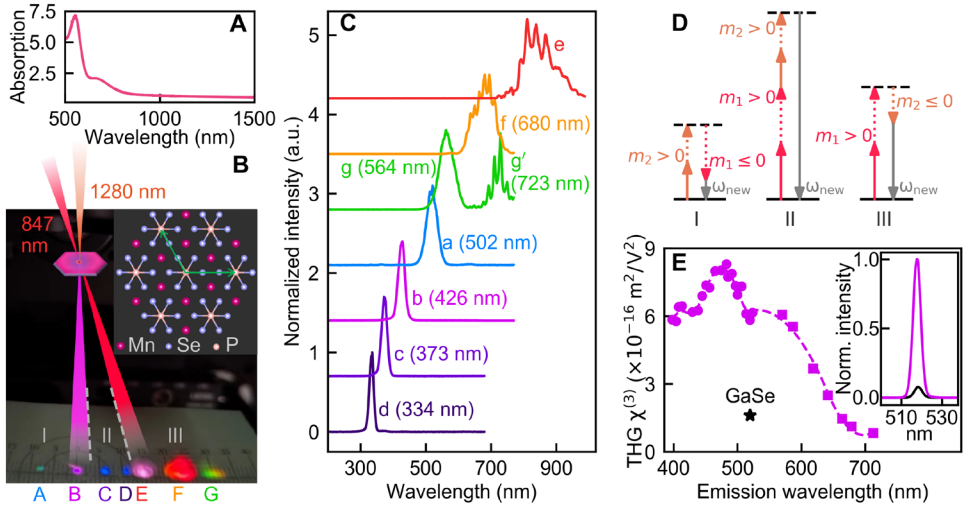

Fig. 1. Optical wave mixing effects in $MnPSe_3$. (**A**) Absorption spectrum of $MnPSe_3$ sample calculated as −ln (*T*), where *T* is the measured broadband transmission ratio (see Materials and Methods). (**B**) View of the nonlinear wave mixing signals of the ~20-μm $MnPSe_3$ bulk. Beams D (334 nm) and C (373 nm) are in the ultraviolet range but were seen on the paper because of the fluorescent whitening agents inside the paper. The photo was taken by a cell phone camera. The inset shows the in-plane structure with green arrows representing the *a* and *b* axes. (**C**) Normalized spectra for beams A to G, vertically shifted for clarity. The signals located at longer than 600 nm contain split sharp peaks that are likely caused by interference effect from the bulk flake sample (see section S2). a.u., arbitrary units. (**D**) Schematics of wave mixing processes of different (m_1, m_2) channels, corresponding to the three regions in (B). (**E**) $\chi^{(3)}$ as a function of emission wavelength obtained by measuring wavelength-dependent THG spectrum (see Materials and Methods and section S4). The dashed line is a guide-to-the-eye. The circle and square markers are measured with the signal and idler output of an optical parametric amplifier. The black star denotes the $\chi^{(3)}$ value of GaSe. Inset: Black and magenta lines represent the THG response measured on 80-nm-thick GaSe (black line) and $MnPSe_3$ (magenta line) films, both are normalized by the peak intensity of $MnPSe_3$.

Table 1. Different nonlinear wave mixing channels. Calculated and measured energies for nonlinear wave mixing processes of third order ($m = 3$) and fifth order ($m = 5$). (m_1, m_2) values leading to $m_1\omega_1 + m_2\omega_2 < 0$ are invalid and not listed in the table. See section S3 for more details.

$m = 3$, FWM	
(m_1, m_2) channels	Corresponding peaks and measured energy (eV)
(0,3)	Peak b of beam B, 2.91 eV (426 nm)
(1,2)	Peak c of beam C, 3.2 eV (373 nm)
(2,1)	Peak d of beam D, 3.71 eV (334 nm)
(2,−1)	Peak f of beam F, 1.82 eV (680 nm)
Others: (−1,2) and (3,0), of 300- to 980-nm range	
$m = 5$, six-wave mixing	
(m_1, m_2) channels	Corresponding peaks and measured energy (eV)
(−1,4)	Peak a of beam A, 2.47 eV (502 nm)
(3,−2)	Peak g of beam G, 2.2 eV (564 nm)
Others: (0,5), (1,4), (2,3), (2,−3), (3,2), (4,1), (4,−1), and (5,0), of 300- to 980-nm range	

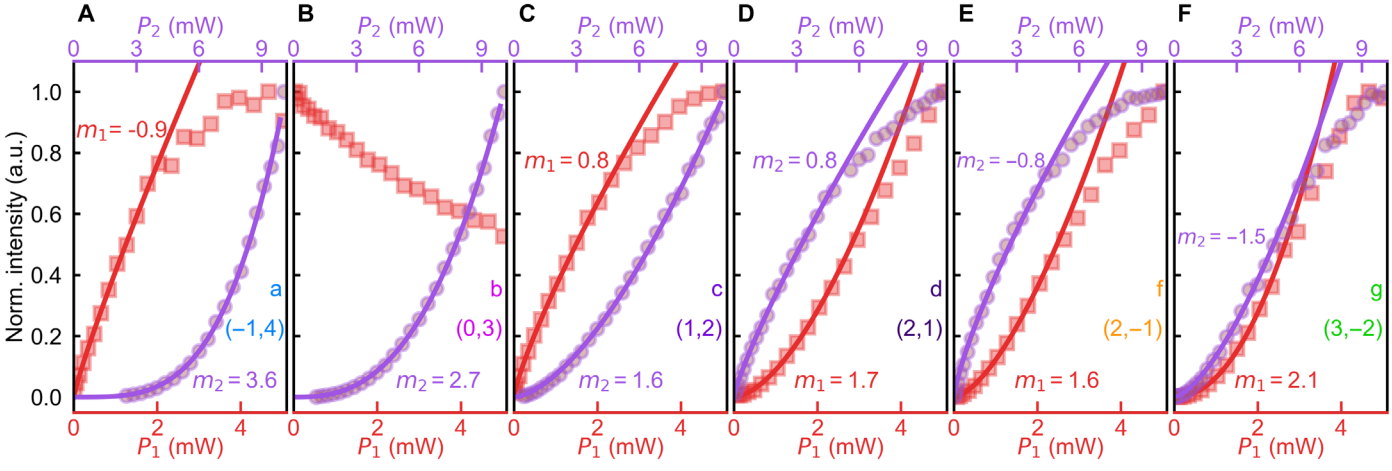

Fig. 2. Excitation power dependence. (**A** to **F**) Intensity of different nonlinear wave mixing signals as a function of 847-nm excitation power P_1 and 1280-nm excitation power P_2 measured on the bulk $MnPSe_3$ sample. The red and purple markers represent the signal intensities when solely decreasing P_1 and P_2, respectively. Solid lines are fits to the data. Given the nonperturbative behavior, the red lines in all panels are fitted only with data of $P_1 \leq 2$ mW, the purple lines in (D) to (F) are fitted only with data of $P_2 \leq 5$ mW.

both in the linear scale plot (Fig. 2) or log-log scale plot (fig. S5). In addition, the THG intensity of 1280-nm laser, which, in principle, should be independent of the 847-nm laser power, is reduced nearly by half at maximum power of 847 nm (Fig. 2B). This reveals a transient response of the THG to the occurrence of nondegenerate wave mixing near time zero, which we will discuss later.

In many HHG studies, nonperturbation in harmonic generation process leads to intensity dependence below the power-law scale of the harmonic order (*32*–*34*), so one may attribute the saturation to the nonperturbative response. However, our measurement was performed with quite low excitation intensity (on the order of 0.01 TW/cm^2) and near-infrared photon energy, leading to low ponderomotive energy and small nonperturbative intensity parameter (see section S5), which usually hold for the perturbation regime. If the saturation is related to nonperturbation, then it may indicate the early-stage crossover from perturbation to nonperturbation, which happens at low excitation density owing to the large multiphoton transition cross section. There are also other possible sources for the saturation feature. One possible source could be nonlinearity of the photoinduced dynamics. In some pump-probe studies, the nonlinearity in the kinetics of the pump excited states has led to saturation in transient photoconductivity (*35*, *36*). In nonlinear spectroscopy, the kinetics of the intermediate states of the multiphoton transition process may also host nonlinearity (*16*, *29*). A related example observed in nondegenerate wave mixing measurement is that photoexcited transient excitonic states have lifetime with nontrivial dependence with excitation powers (*16*). Another source of saturation could be the nonlinearity in the absorption of excitation photons, which we discuss later in the temporal measurement results.

A typical 2D material with highest third-order susceptibility is GaSe [see table 1 in (*6*) and table 4.1.2 in (*1*) for summaries of nonlinear susceptibilities of various materials], with $\chi^{(3)} = 1.6 \times 10^{-16}$ m^2/V^2 at 520-nm emission wavelength. In our experiment, different FWM processes are related to different $\chi^{(3)}$ values. We compared the THG efficiency of GaSe and $MnPSe_3$ thin films at 520-nm emission wavelength and also estimated the wavelength-dependent THG $\chi^{(3)}$

of $MnPSe_3$ as shown in Fig. 1E (see section S4 for details). $\chi^{(3)}$ increases substantially with decreasing wavelength over a range around 600 nm, near the fine features of absorption enhancement in the spectra of Fig. 1A. Another increase in THG $\chi^{(3)}$ appears around 490 nm, which may be related to the optical gap of $MnPSe_3$. These increases in $\chi^{(3)}$ near the absorption features hints that the increased density of intermediate states for the multiphoton transition processes enhances the conversion efficiency for the nonlinear THG process. Near 470 nm, $MnPSe_3$ shows $\chi^{(3)}$ values near the order of 1×10^{-15} m^2/V^2. The values reach near the highest record of third-order susceptibilities in 2D materials in the optical range (*6*).

Note that there are distinct examples of extremely large third-order susceptibilities of graphene with terahertz excitation. One is the THG susceptibility of ~10^{-9} m^2/V^2 when excited by very-low-frequency terahertz sources (*37*). Another is the FWM third-order susceptibility of ~10^{-10} m^2/V^2 measured specifically in magnetic fields with higher terahertz frequency in resonance with the 78-meV Landau levels (*38*). Nevertheless, these examples do not diminish the importance of our finding. Nonlinear optical responses in the optical range or terahertz range, with huge difference in the excitation photon energies and related nonlinear light-matter interacting mechanisms, can be viewed as two quite distinct fields. Terahertz nonlinear optics faces much limitation due to the weak strength of light sources and long wavelength unsuitable for state-of-the-art nanoapplications, whereas optical-range nonlinear optics have been playing vast roles in both traditional and next-generation optical research and applications. Besides, the large optical nonlinearity in graphene and $MnPSe_3$ should be from different origins. $MnPSe_3$ is an insulator with quite a large bandgap. Graphene is intrinsically a semimetal with a zero bandgap. The profound high-order nonlinear optical responses are closely related to the linear dispersion, which will also cause inevitably heavy absorption under high-power excitation.

For the bulk sample, beam F [the (2,−1) channel] is the strongest among all wave mixing beams, with ~2-μW power that can be directly measured by a power meter. This yields an FWM efficiency near the order of 10^{-4}. As for the six-wave mixing outputs, beam G [the (3,−2) channel] shows the highest efficiency near the order of 10^{-6}. We compared the wave mixing efficiency of the bulk sample with two other films of about 1 μm and 100 nm in thicknesses (Fig. 3). The difference in wave mixing efficiency is insignificant between the bulk sample and the 1-μm film. For the 100-nm film, signals f and g are lowered by one to two orders of magnitude, while others change slightly. The intensity of nonlinear wave mixing signals is influenced by material thickness through several possible factors. One is the enhanced absorption of photons with increasing thickness (*13*, *14*). Another important factor is phase-matching condition (*39*). For the thin films within the order of 100 nm that is much shorter than the coherence length, phase match is usually automatically satisfied, and the efficiency should grow quadratically with layer numbers in the absence of absorption. For thicker films, phase match, if not accidently satisfied, usually requires fine tuning of the refractive index between the incident and signal pulses. Only with phase match will the efficiency continue growing quadratically with thickness (*14*, *40*). Otherwise, phase mismatching, which is the case for our measurements, will lead to nonmonotonically oscillating dependence of the conversion efficiency to increasing thickness. There also exist other factors affecting the thickness dependence of wave mixing efficiency, such as multireflection due to interfaces (*41*). Overall, the wave mixing efficiency on samples with different thicknesses in our study should be a joint outcome of these multiple factors, as we specifically demonstrated for the THG signals in section S6. The efficiency could be largely improved in $MnPSe_3$ samples in the future by optimizing these factors, such as fine tuning of phase-matching condition.

We compared the wave mixing efficiency of $MnPSe_3$ with other nonlinear optical materials. $LiNbO_3$ is a typical bulk nonlinear crystal and also commonly used for engineering third-order nonlinear responses through cascaded second-order processes (*11*, *12*, *42*). It also yields profound second-order SFG signal seen as the green SFG speckle shown in Fig. 3A. Fused silica is commonly used for optical elements and, here, used as substrates of all thin films. WS_2 is a typical 2D vdW material with large nonlinear susceptibility (*6*). The overall efficiency of different wave mixing processes in $LiNbO_3$ and

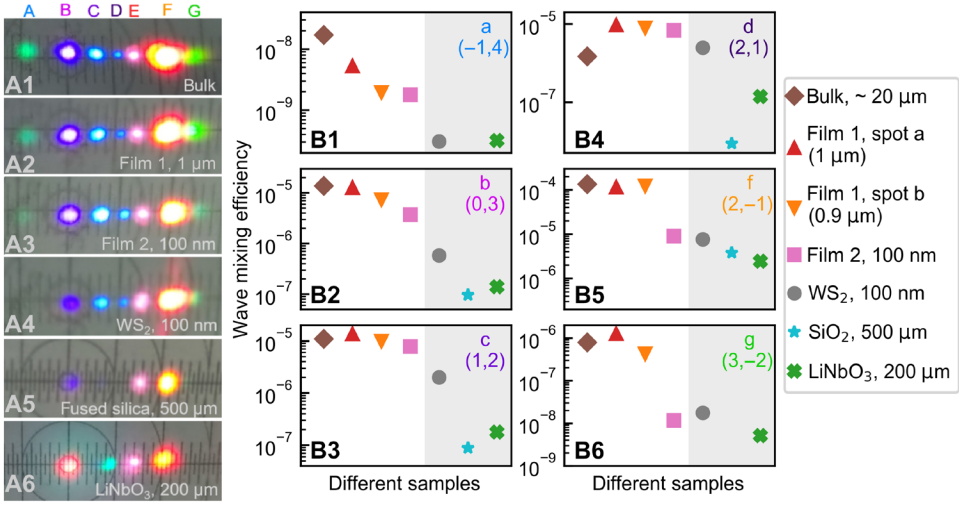

Fig. 3. Nonlinear wave mixing efficiency in different samples. (**A1** to **A6**) Outgoing beams directly observed on a paper card behind different samples. Note that the green speckles for WS_2 and $LiNbO_3$ samples are the SFG of the 847- and 1280-nm lasers. (**B1** to **B6**) Efficiency of different nonlinear wave mixing processes of different samples. The measurements were performed with excitation powers $P_1 = 5$ mW and $P_2 = 10$ mW.

silica bulks falls below $MnPSe_3$ films by orders of magnitude. For the 100-nm WS_2 film, the efficiency of signals a to c falls far below the 100-nm $MnPSe_3$ film, while the efficiency of other signals differs slightly between the two samples. Our comparison renders $MnPSe_3$ to be among the set of the most efficient materials for odd-order nonlinear wave mixing.

The large optical nonlinearity and giant wave mixing effect of $MnPSe_3$ suggest its potential as multicolor nonlinear optical waveguide. Currently, nonlinear optical waveguides based on 2D materials usually operate in single-color mode with monochronic laser excitation and SHG (*41*, *43*). Figure 4A illustrates a multicolor waveguided nonlinear optical wave mixing regime under noncollinear geometry. In our experiment, two laser beams with wavelength of ~800 and ~1300 nm were displaced away from the center of a reflective objective. To achieve coupling into the waveguide, the two excitation beams are focused onto the same point on one side of the $MnPSe_3$ flake with slightly different incident angles. The multiple nonlinear wave mixing processes in $MnPSe_3$ generate multicolor outputs simultaneously with different momenta, which can propogate seperately inside the waveguide in the noncollinear geometry.

As shown in Fig. 4D, the FWM outputs of (2,−1) and (0,3) channels travel over a propagation length of ~60 μm along different pathways and are collected from the opposite edge with the same objective. Our results demonstrate the applicational potential of $MnPSe_3$ as efficient on-chip nonlinear waveguide, which is essential to generate new frequencies and quantum states of light. The light of different channels could travel along distinct pathways by deliberately designed incident angles into the waveguide. The generated frequencies can be spatially separated easily for signal detection or modulation without integrated filter, which is promising for future nonlinear wavelength division multiplexing techniques.

To explore the temporal dynamics of the nonlinear responses, we performed time-resolved measurements. Figure 5 (A1 to A7) shows the spectra for beams A to G as a function of $\Delta t = t_{847} - t_{1280}$. The nondegenerate wave mixing signals d, c, a, g, and f appear only near $\Delta t = 0$. The THG signal b and the 847-nm transmission signal e are present at all times. The transmission signal peak e is reduced by about 10% at $\Delta t = 0$ (Fig. 5C), which is much larger than the transient absorption change in common pump probe experiments. This suggests that nonlinear wave mixing processes with high conversion efficiency heavily consume the excitation photons, leading to large transient absorption. The THG signal b is reduced nearly by half at $\Delta t = 0$, which indicates that the multiple efficient wave mixing processes may compete with each other for excitation photons and lead to mutual suppression. Moreover, the time evolution of signals b and e shows dissipative behaviors. Here, $\Delta t > 0$ (<0) means that the 1280-nm pulses arrive before (after) the 847-nm pulses. At negative Δt, signal b relaxes back to only about 80% of the original intensity. At positive Δt, signal e relaxes back to about 95% of the original intensity. While nonlinear wave mixing is usually regarded as a nondissipative instantaneous process occurring on the short timescale of the pulse duration, the dissipative behaviors hint that photoinduced carriers are generated along with the multiphoton processes of strong nonlinear wave mixing. The saturation behavior shown in Fig. 2 could also be caused by the nonlinear photon absorption. As the nonlinear conversion efficiency grows with increasing excitation

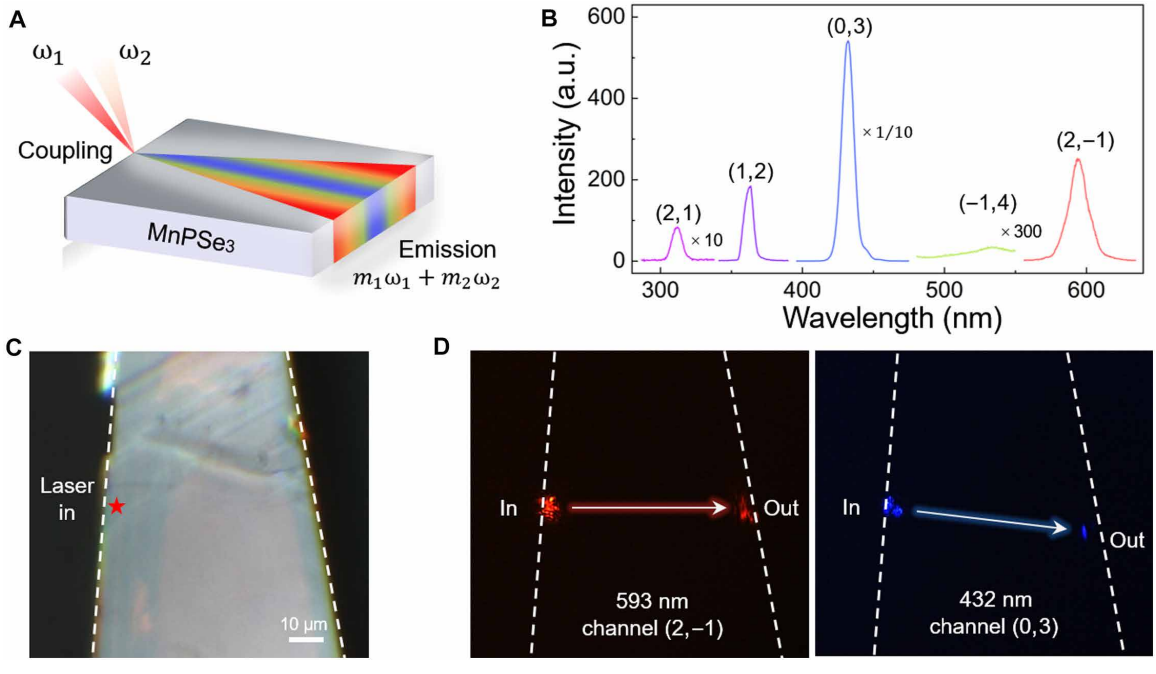

Fig. 4. Waveguided nonlinear optical wave mixing. (**A**) Schematic of light coupling and emission of the waveguided nonlinear optical wave mixing in noncollinear geometry. Two incident excitation beams at ~800 and ~1300 are displaced away from the center of a reflective objective to achieve coupling on a side of the $MnPSe_3$ flake in a noncollinear geometry. (**B**) Spectra of the nonlinear four- and six-wave mixing in the $MnPSe_3$ flake when setting the two excitation beams collinear and at normal incidence. The different wave mixing channels are denoted at the top of each peak. (**C**) Optical image of the $MnPSe_3$ flake used as the waveguide. (**D**) Optical images of the coupling and emission of different wave mixing channels that take place simultaneously in the waveguide. In the noncollinear geometry, the different wave mixing signals travel along distinct pathways and can be collected at different emission points. The two images are photographed with suitable bandpass filters.

powers, the absorption may become more intense, leading to a slow down of the intensity of wave mixing signals. Besides, the competition and mutual suppression of different wave mixing channels could also result in saturation.

At positive time delays, two unexpected dynamical signals of new energies (denoted as a′ and g′ in Fig. 5, A4 and A5) appear with the two six-wave mixing signals measured at speckles A and G but with new energies. g′ extends longer in time than the wave mixing peak g. a′ appears far away from time zero and shows an oscillatory behavior with 11-THz frequency (Fig. 5, D and E). It is also interesting that a′ and g′ signals vary a lot among different spots on the bulk sample and are absent in the flat films with thicknesses of 1 μm and 100 nm (section S7). This indicates that a′ and g′ signals are not only dependent on the material itself but also extremely sensitive to environmental perturbation, including the thickness and geometric structure of the bulk sample with steps or winkles inside. The exact origin of signals a′ and g′ deserves further investigation, and, here, we propose a possible qualitative explanation related to the soliton evolution mechanism. Different from the fundamental soliton whose shape and amplitude remain unchanged with propagation, the high-order soliton exhibits periodical evolution of shape and spectra with time and distance, resulted from the interactions of self-phase modulation and dispersion (*44*, *45*). Note that even slight perturbations to the materials' dispersive and nonlinear responses would break the symmetry of the evolution; hence, the higher-order soliton will undergo a process called soliton fission (*46*), where the initial pulse splits into a train of individual fundamental soliton pulses. As for the newly formed soliton, the effect of inelastic light scattering within the bandwidth of each soliton (also known as intrapulse Raman scattering) generates the long wavelength side of the continuum, which is also the key to understand the supercontinuum generation process (*45*, *46*).

DISCUSSION

The MPX_3 family contains members with different electronic structure and magnetism. We also observed strong wave mixing responses in two other members ($MnPS_3$ and $NiPS_3$; section S8), suggesting it as a universal property of the MPX_3 compounds. It is worth investigating how the nonlinear wave mixing signals depend on the material-specific electronic and magnetic properties. This would also help to theoretically address the exact origin of this large optical nonlinearity. Given the layered nature of MPX_3 materials, state-of-the-art nanofabrication and integration techniques, such as vdW engineering (e.g., heterostructuring and moiré structuring) (*9*, *47*), optical coupling to cavities, and waveguides (*25*, *41*), would be promising to enhance the wave mixing efficiency and engineer nonlinear photonic devices. Our findings not only add a member to the collection of 2D materials hosting large optical nonlinearities but also inspire future research in the following perspectives.

Magnetism has always been a research focus of MPX_3 materials and greatly modifies the optical properties (*17*–*29*). It is worth studying how the nonlinear wave mixing will depend on the magnetic properties. So far, SHG has become powerful for probing magnetic symmetries in 2D materials (*27*–*29*, *48*), but how the high-order nonlinearities will response to magnetic orders remains elusive. The study of high-order nonlinearities in the AFM phases of MPX_3 materials will add insights to such knowledge, with respect to this family and magnetic systems in general. Besides magnetism effects, another intriguing question is whether the wave mixing processes present

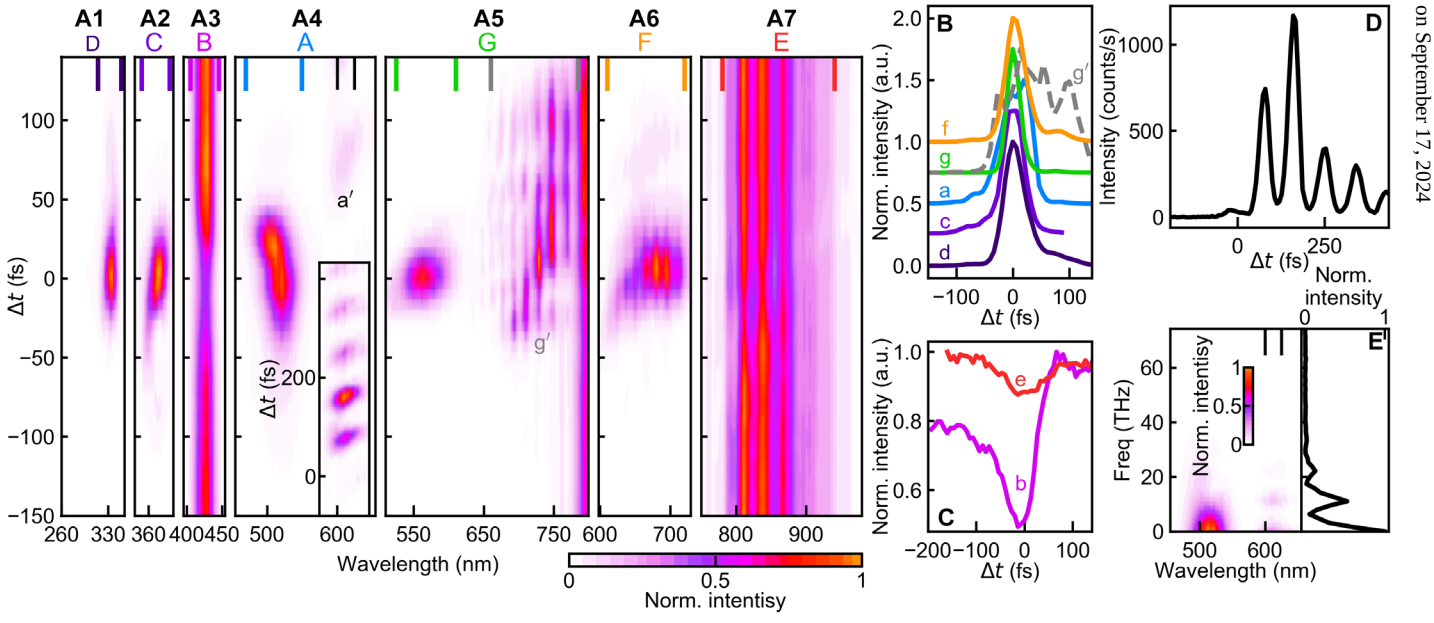

Fig. 5. Temporal dynamics. (**A1** to **A7**) Time-dependent spectra of outgoing beam D, C, B, A, G, F, and E, respectively, measured on the bulk $MnPSe_3$ sample. (**B**) Time evolution of integrated intensity of the nondegenerate wave mixing peaks d, c, a, g (and g′), and f. Each curve is normalized by the maximum value and vertically shifted for clarity. (**C**) Time evolution of integrated intensity of peaks d and e, each normalized by the maximum value. (**D**) Time evolution of integrated intensity of peak a′. The integration ranges in (B) to (D) are marked by the colored ticks on top of the axes in (A1) to (A7). (**E**) Left: Fast Fourier transformation of the time-dependent spectra measured at speckle A presented in (A4). Right: Integrated fast Fourier transformation intensities in the range of 600 to 625 nm of the left panels, normalized by the maximum value.

any excitonic effects when varying excitation laser wavelengths (*49*, *50*), given the general fact that the many-body excitons strongly influence the optical properties of MPX_3 materials (*20*–*22*, *51*, *52*) and that resonance to different excitonic states can modify the temporal dynamics of wave mixing processes (*16*) or activate the precession of magnons (*22*). The multiple (m_1, m_2) wave mixing channels in MPX_3 compounds offer unique advantages for clarifying the nonlinear light-matter interactions with different multiphoton excitonic quantum transition paths (*16*), while the many-body exciton nature may further enrich the interacting mechanism.

Large odd-order nonlinear susceptibilities in the MPX_3 materials can be exploited in other nonlinear optical effects, such as self-phase modulation, saturable absorption, and coherent photon conversion, which are all important for nonlinear optical and nanophotonic applications (*53*). Besides, one could try to reach higher-order nonlinear wave mixing effects, such as high-order sideband generation and HHG, which have become an emerging field recently for studying band structure properties (*33*, *54*, *55*), field-driven ultrafast electron dynamics (*16*, *56*–*58*), and optical band engineering (*59*). The endeavor toward higher-order wave mixing responses in correlated magnetic materials MPX_3 may give new insight to this field.

In all, we found giant four-wave and six-wave mixing effects in a wide spectral range from ultraviolet to visible in $MnPSe_3$ (and other transition metal phosphorous trichalcogenides), rendering it to be a model 2D system of large odd-order optical nonlinearities. Our work highlights the great potential of transition metal phosphorous trichalcogenide family for exploring nonlinear optical processes from both fundamental scientific and applicational points of view. Future research is promising for clarifying the nonlinear light-matter interaction mechanisms in the correlated 2D systems, reaching higher conversion efficiency and engineering new optical devices for nonlinear photonic applications.

MATERIALS AND METHODS

Sample preparation

Single crystals of $MnPSe_3$ and $MnPS_3$ were prepared by a chemical vapor transport method. A mixture of Mn (99.9%), P (99%), Se/S (99.9%) with the molar ratios of Mn:P:Se/S = 1:1:3 and additional iodine as transport agent. The mixture was subsequently sealed in an evacuated quartz tube, which was placed in a two-zone furnace. The reaction zone was heated to 973 K and held for 5 days, with the growth zone held at 1023 K. Then, we exchanged temperature gradient of the two zones and kept for 3 weeks. Then, the quartz tube was naturally cooled down to room temperature. Last, $MnPSe_3$ and $MnPS_3$ platelet-shaped crystals in several millimeter sizes were obtained in the growth zone.

The thin $MnPSe_3$ films (film 1 and film 2 in Fig. 3 and also shown in fig. S6) were obtained by mechanical exfoliation on fused silica substrates. In this study, there are other materials used as comparisons to $MnPSe_3$ samples. $LiNbO_3$ and fused silica substrates were commercially purchased. The 100-nm WS_2 film was grown by the chemical vapor deposition method and mechanical exfoliation on fused silica substrates. The 80-nm GaSe film was obtained by mechanical exfoliation on fused silica substrate.

Nonlinear optical wave mixing

The 847- and 1280-nm lasers were generated by a LIGHT CONVERSION ORPHEUS-F hybrid optical parametric amplifier, pumped by 1024-nm laser generated by a LIGHT CONVERSION PHAROS Yb:KGW laser system. The repetition rate was 50 kHz. The two lasers were focused onto the sample in a noncollinear geometry by two optical lens. The diameter of the laser spot at the focus was about 100 μm. The time resolution of the setup was ~43 fs. The two incident lasers were linearly polarized along *s* direction. The spectra of wave mixing signals were measured by an NOVA high-sensitive spectrometer, IdeaOptics, China. The spectrometer covers the 200- to 980-nm range. When measuring signals below 650 nm, short-pass color-glass filters were placed before the spectrometer to eliminate the contamination of spectrum by the scattered 847-nm excitation laser. The short-pass filters do not extend to infinitely short wavelengths but show cutoff near 300 nm. Therefore, the overall accessible wavelength range of the measurement setup was 300 to 980 nm. See fig. S1 for the schematic of the optical setup.

Waveguided nonlinear optical wave mixing

Two laser beams with wavelengths of ~800 and ~1300 nm were displaced away from the center of the reflective objective (40×, numerical aperture = 0.5) and focused obliquely on the sample ($MnPSe_3$ flake on fused silica substrate) in noncollinear manner. The generated wave mixing signals traveled to the opposite edge of the flake and were collected by the same objective. The coupling and emission images were photographed using suitable filters.

Broadband transmission measurement

The absorption spectrum (shown in Fig. 1A) were obtained from broadband transmission spectrum measured by a Bruker 80-V Fourier transform infrared spectrometer. A sample with a thickness of ~100 μm and a lateral size large than 3 mm was glued on a copper platform with a hollow hole. We measured the transmitted spectra of the sample and another hole with the same diameter for comparison. The transmission ratio T was obtained by dividing the spectra of the sample and the hole.

Wavelength-dependent THG

The dependence on THG emission wavelengths of $\chi^{(3)}$ shown in Fig. 1E was derived from THG measurements at varying excitation wavelengths. We used a Spectra-Physics TOPAS Prime optical parametric amplifier to generate excitation laser from 1200 to 2000 nm at 1-kHz repetition rate. The excitation laser was focused onto the $MnPSe_3$ 100-nm film sample using an optical lens with 125 mm in focal length. The THG signals centered at emission wavelengths shorter (longer) than 550 nm were measured with the signal (idler) output of the optical parametric amplifier. The power of incident excitation laser was always kept at 0.4 mW. To evaluate the THG $\chi^{(3)}$ of $MnPSe_3$, we first compare the 520-nm THG signal intensity of $MnPSe_3$ and GaSe films both of 80 nm in thickness and calculate the $\chi^{(3)}$ of $MnPSe_3$ at 520 nm using the measured intensity ratio and the reported refractive index of $MnPSe_3$ (*60*) and GaSe (*61*, *62*). Then, we can calculate the wavelength-dependent $\chi^{(3)}$ through the wavelength-dependent THG intensities. The detailed calculation process is shown in section S4.

Thickness dependence of THG

The various $MnPSe_3$ films of different thicknesses are fabricated through mechanical exfoliation on fused silica substrates. The measurements was carried out on a distinct optical setup with 1550-nm excitation laser and optical focusing with 20× objectives with 0.4

numerical aperture. The focused laser spot is about 5 μm in diameter. We numerically simulated the THG intensity using a frequency-domain finite-element method. The real and imaginary part of the complex refractive index of $MnPSe_3$ at different wavelength is obtained from previous report (*60*).

Supplementary Materials

This PDF file includes:

Supplementary Sections S1 to S8
Figs. S1 to S8
Table S1

REFERENCES AND NOTES

1. R. W. Boyd, *Nonlinear Optics* (Academic Press, 2007).
2. Y. Shen, *The Principles of Nonlinear Optics* (Wiley Press, 1984).
3. M. Duelli, G. Montemezzani, M. Zgonik, P. Günter, "Photorefractive memories for optical processing" in *Nonlinear Optical Effects and Materials* (Springer, 2000), pp. 375–436.
4. U. Keller, Recent developments in compact ultrafast lasers. *Nature* **424**, 831–838 (2003).
5. E. Garmire, Nonlinear optics in daily life. *Opt. Express* **21**, 30532–30544 (2013).
6. A. Autere, H. Jussila, Y. Dai, Y. Wang, H. Lipsanen, Z. Sun, Nonlinear optics with 2D layered materials. *Adv. Mater.* **30**, e1705963 (2018).
7. D. E. Chang, V. Vuletić, M. D. Lukin, Quantum nonlinear optics—Photon by photon. *Nat. Photonics* **8**, 685–694 (2014).
8. A. W. Elshaari, W. Pernice, K. Srinivasan, O. Benson, V. Zwiller, Hybrid integrated quantum photonic circuits. *Nat. Photonics* **14**, 285–298 (2020).
9. Y. Liu, Y. Huang, X. Duan, Van der Waals integration before and beyond two-dimensional materials. *Nature* **567**, 323–333 (2019).
10. B. Guo, Q.-L. Xiao, S.-H. Wang, H. Zhang, 2D layered materials: Synthesis, nonlinear optical properties, and device applications. *Laser Photon. Rev.* **13**, 1800327 (2019).
11. M. Hunault, H. Takesue, O. Tadanaga, Y. Nishida, M. Asobe, Generation of time-bin entangled photon pairs by cascaded second-order nonlinearity in a single periodically poled $LiNBO_3$ waveguide. *Opt. Lett.* **35**, 1239–1241 (2010).
12. Z. Zhang, C. Yuan, S. Shen, H. Yu, R. Zhang, H. Wang, H. Li, Y. Wang, G. Deng, Z. Wang, L. You, Z. Wang, H. Song, G. Guo, Q. Zhou, High-performance quantum entanglement generation via cascaded second-order nonlinear processes. *npj Quantum Inf.* **7**, 123 (2021).
13. E. Hendry, P. J. Hale, J. Moger, A. K. Savchenko, S. A. Mikhailov, Coherent nonlinear optical response of graphene. *Phys. Rev. Lett.* **105**, 097401 (2010).
14. S.-Y. Hong, J. I. Dadap, N. Petrone, P. C. Yeh, J. Hone, R. M. Osgood, Optical third-harmonic generation in graphene. *Phys. Rev. X* **3**, 021014 (2013).
15. J. Hernandez-Rueda, M. L. Noordam, I. Komen, L. Kuipers, Nonlinear optical response of a WS_2 monolayer at room temperature upon multicolor laser excitation. *ACS Photonics* **8**, 550–556 (2021).
16. J. M. Bauer, L. Chen, P. Wilhelm, K. Watanabe, T. Taniguchi, S. Bange, J. M. Lupton, K.-Q. Lin, Excitonic resonances control the temporal dynamics of nonlinear optical wave mixing in monolayer semiconductors. *Nat. Photonics* **16**, 777–783 (2022).
17. S. Y. Kim, T. Y. Kim, L. J. Sandilands, S. Sinn, M.-C. Lee, J. Son, S. Lee, K.-Y. Choi, W. Kim, B.-G. Park, C. Jeon, H.-D. Kim, C.-H. Park, J.-G. Park, S. J. Moon, T. W. Noh, Charge-spin correlation in van der Waals antiferromagnet $NiPS_3$. *Phys. Rev. Lett.* **120**, 136402 (2018).
18. E. Ergeçen, B. Ilyas, D. Mao, H. C. Po, M. B. Yilmaz, J. Kim, J.-G. Park, T. Senthil, N. Gedik, Magnetically brightened dark electron-phonon bound states in a van der Waals antiferromagnet. *Nat. Commun.* **13**, 98 (2022).
19. X. Wang, J. Cao, Z. Lu, A. Cohen, H. Kitadai, T. Li, Q. Tan, M. Wilson, C. H. Lui, D. Smirnov, S. Sharifzadeh, X. Ling, Spin-induced linear polarization of photoluminescence in antiferromagnetic van der Waals crystals. *Nat. Mater.* **20**, 964–970 (2021).
20. S. Kang, K. Kim, B. H. Kim, J. Kim, K. I. Sim, J.-U. Lee, S. Lee, K. Park, S. Yun, T. Kim, A. Nag, A. Walters, M. Garcia-Fernandez, J. Li, L. Chapon, K.-J. Zhou, Y.-W. Son, J. H. Kim, H. Cheong, J.-G. Park, Coherent many-body exciton in van der Waals antiferromagnet $NiPS_3$. *Nature* **583**, 785–789 (2020).
21. K. Hwangbo, Q. Zhang, Q. Jiang, Y. Wang, J. Fonseca, C. Wang, G. M. Diederich, D. R. Gamelin, D. Xiao, J. H. Chu, W. Yao, X. Xu, Highly anisotropic excitons and multiple phonon bound states in a van der Waals antiferromagnetic insulator. *Nat. Nanotechnol.* **16**, 655–660 (2021).
22. C. A. Belvin, E. Baldini, I. O. Ozel, D. Mao, H. C. Po, C. J. Allington, S. Son, B. H. Kim, J. Kim, I. Hwang, J. H. Kim, J. G. Park, T. Senthil, N. Gedik, Exciton-driven antiferromagnetic metal in a correlated van der Waals insulator. *Nat. Commun.* **12**, 4837 (2021).
23. Z. Ni, A. V. Haglund, H. Wang, B. Xu, C. Bernhard, D. G. Mandrus, X. Qian, E. J. Mele, C. L. Kane, L. Wu, Imaging the Néel vector switching in the monolayer antiferromagnet $MnPSe_3$ with strain-controlled ising order. *Nat. Nanotechnol.* **16**, 782–787 (2021).
24. K. Kim, S. Y. Lim, J. U. Lee, S. Lee, T. Y. Kim, K. Park, G. S. Jeon, C. H. Park, J. G. Park, H. Cheong, Suppression of magnetic ordering in XXZ-type antiferromagnetic monolayer $NiPS_3$. *Nat. Commun.* **10**, 345 (2019).
25. H. Zhang, Z. Ni, C. E. Stevens, A. Bai, F. Peiris, J. R. Hendrickson, L. Wu, D. Jariwala, Cavity-enhanced linear dichroism in a van der Waals antiferromagnet. *Nat. Photonics.* **16**, 311–317 (2022).
26. Q. Zhang, K. Hwangbo, C. Wang, Q. Jiang, J.-H. Chu, H. Wen, D. Xiao, X. Xu, Observation of giant optical linear dichroism in a zigzag antiferromagnet $FePS_3$. *Nano Lett.* **21**, 6938–6945 (2021).
27. Z. Ni, H. Zhang, D. A. Hopper, A. V. Haglund, N. Huang, D. Jariwala, L. C. Bassett, D. G. Mandrus, E. J. Mele, C. L. Kane, L. Wu, Direct imaging of antiferromagnetic domains and anomalous layer-dependent mirror symmetry breaking in atomically thin $MnPS_3$. *Phys. Rev. Lett.* **127**, 187201 (2021).
28. H. Chu, C. J. Roh, J. O. Island, C. Li, S. Lee, J. Chen, J.-G. Park, A. F. Young, J. S. Lee, D. Hsieh, Linear magnetoelectric phase in ultrathin $MnPS_3$ probed by optical second harmonic generation. *Phys. Rev. Lett.* **124**, 027601 (2020).
29. J.-Y. Shan, M. Ye, H. Chu, S. Lee, J.-G. Park, L. Balents, D. Hsieh, Giant modulation of optical nonlinearity by floquet engineering. *Nature* **600**, 235–239 (2021).
30. F. Wang, T. A. Shifa, P. Yu, P. He, Y. Liu, F. Wang, Z. Wang, X. Zhan, X. Lou, F. Xia, J. He, New frontiers on van der Waals layered metal phosphorous trichalcogenides. *Adv. Funct. Mater.* **28**, 1802151 (2018).
31. V. Grasso, L. Silipigni, Optical absorption and reflectivity study of the layered $MnPSe_3$ seleniophosphate. *J. Opt. Soc. Am. B* **16**, 132–136 (1999).
32. N. Yoshikawa, T. Tamaya, K. Tanaka, High-harmonic generation in graphene enhanced by elliptically polarized light excitation. *Science* **356**, 736–738 (2017).
33. H. Liu, Y. Li, Y. S. You, S. Ghimire, T. F. Heinz, D. A. Reis, High-harmonic generation from an atomically thin semiconductor. *Nat. Phys.* **13**, 262–265 (2017).
34. Y.-Y. Lv, J. Xu, S. Han, C. Zhang, Y. Han, J. Zhou, S.-H. Yao, X.-P. Liu, M.-H. Lu, H. Weng, Z. Xie, Y. B. Chen, J. Hu, Y.-F. Chen, S. Zhu, High-harmonic generation in Weyl semimetal β-WP_2 crystals. *Nat. Commun.* **12**, 6437 (2021).
35. D. G. Sahota, R. Liang, M. Dion, P. Fournier, H. A. Dąbkowska, G. M. Luke, J. S. Dodge, Many-body recombination in photoexcited insulating cuprates. *Phys. Rev. Res.* **1**, 033214 (2019).
36. J. C. Petersen, A. Farahani, D. G. Sahota, R. Liang, J. S. Dodge, Transient terahertz photoconductivity of insulating cuprates. *Phys. Rev. B* **96**, 115133 (2017).
37. H. A. Hafez, S. Kovalev, J. C. Deinert, Z. Mics, B. Green, N. Awari, M. Chen, S. Germanskiy, U. Lehnert, J. Teichert, Z. Wang, K. J. Tielrooij, Z. Liu, Z. Chen, A. Narita, K. Müllen, M. Bonn, M. Gensch, D. Turchinovich, Extremely efficient terahertz high-harmonic generation in graphene by hot Dirac fermions. *Nature* **561**, 507–511 (2018).
38. J. C. König-Otto, Y. Wang, A. Belyanin, C. Berger, W. A. de Heer, M. Orlita, A. Pashkin, H. Schneider, M. Helm, S. Winnerl, Four-wave mixing in landau-quantized graphene. *Nano Lett.* **17**, 2184–2188 (2017).
39. C. Li, *Nonlinear Optics: Principles and Applications* (Springer Singapore, 2016).
40. H. Hong, C. Huang, C. Ma, J. Qi, X. Shi, C. Liu, S. Wu, Z. Sun, E. Wang, K. Liu, Twist phase matching in two-dimensional materials. *Phys. Rev. Lett.* **131**, 233801 (2023).
41. X. Xu, C. Trovatello, F. Mooshammer, Y. Shao, S. Zhang, K. Yao, D. N. Basov, G. Cerullo, P. J. Schuck, Towards compact phase-matched and waveguided nonlinear optics in atomically layered semiconductors. *Nat. Photonics* **16**, 698–706 (2022).
42. S. Arahira, N. Namekata, T. Kishimoto, H. Yaegashi, S. Inoue, Generation of polarization entangled photon pairs at telecommunication wavelength using cascaded $\chi^{(2)}$ processes in a periodically poled $LiNbO_3$ ridge waveguide. *Opt. Express* **19**, 16032–16043 (2011).
43. H. Chen, V. Corboliou, A. S. Solntsev, D.-Y. Choi, M. A. Vincenti, D. de Ceglia, C. de Angelis, Y. Lu, D. N. Neshev, Enhanced second-harmonic generation from two-dimensional $MoSe_2$ on a silicon waveguide. *Light Sci. Appl.* **6**, e17060 (2017).
44. J. M. Dudley, G. Genty, C. Stéphane, *Supercontinuum Generation in Optical Fibers* (Cambridge Univ. Press, 2010).
45. J. M. Dudley, G. Genty, S. Coen, Supercontinuum generation in photonic crystal fiber. *Rev. Mod. Phys.* **78**, 1135–1184 (2006).
46. J. M. Dudley, G. Genty, Supercontinuum light. *Phys. Today* **66**, 29–34 (2013).
47. D. Huang, J. Choi, C.-K. Shih, X. Li, Excitons in semiconductor moiré superlattices. *Nat. Nanotechnol.* **17**, 227–238 (2022).
48. Z. Sun, Y. Yi, T. Song, G. Clark, B. Huang, Y. Shan, S. Wu, D. Huang, C. Gao, Z. Chen, M. McGuire, T. Cao, D. Xiao, W.-T. Liu, W. Yao, X. Xu, S. Wu, Giant nonreciprocal second-harmonic generation from antiferromagnetic bilayer CrI_3. *Nature* **572**, 497–501 (2019).
49. T. Low, A. Chaves, J. D. Caldwell, A. Kumar, N. X. Fang, P. Avouris, T. F. Heinz, F. Guinea, L. Martin-Moreno, F. Koppens, Polaritons in layered two-dimensional materials. *Nat. Mater.* **16**, 182–194 (2017).

50. E. C. Regan, D. Wang, E. Y. Paik, Y. Zeng, L. Zhang, J. Zhu, A. H. MacDonald, H. Deng, F. Wang, Emerging exciton physics in transition metal dichalcogenide heterobilayers. *Nat. Rev. Mater.* **7**, 778–795 (2022).
51. Z. Wang, X.-X. Zhang, Y. Shiomi, T.-H. Arima, N. Nagaosa, Y. Tokura, N. Ogawa, Exciton-magnon splitting in the van der Waals antiferromagnet $MnPS_3$ unveiled by second-harmonic generation. *Phys. Rev. Res.* **5**, L042032 (2023).
52. S. L. Gnatchenko, I. S. Kachur, V. G. Piryatinskaya, Y. M. Vysochanskii, M. I. Gurzan, Exciton-magnon structure of the optical absorption spectrum of antiferromagnetic $MnPS_3$. *Low. Temp. Phys.* **37**, 144–148 (2011).
53. N. K. Langford, S. Ramelow, R. Prevedel, W. J. Munro, G. J. Milburn, A. Zeilinger, Efficient quantum computing using coherent photon conversion. *Nature* **478**, 360–363 (2011).
54. J. B. Costello, S. D. O'Hara, Q. Wu, D. C. Valovcin, L. N. Pfeiffer, K. W. West, M. S. Sherwin, Reconstruction of bloch wavefunctions of holes in a semiconductor. *Nature* **599**, 57–61 (2021).
55. L. Yue, R. Hollinger, C. B. Uzundal, B. Nebgen, Z. Gan, E. Najafidehaghani, A. George, C. Spielmann, D. Kartashov, A. Turchanin, D. Y. Qiu, M. B. Gaarde, M. Zuerch, Signatures of multiband effects in high-harmonic generation in monolayer MoS_2. *Phys. Rev. Lett.* **129**, 147401 (2022).
56. O. Schubert, M. Hohenleutner, F. Langer, B. Urbanek, C. Lange, U. Huttner, D. Golde, T. Meier, M. Kira, S. W. Koch, R. Huber, Sub-cycle control of terahertz high-harmonic generation by dynamical bloch oscillations. *Nat. Photonics* **8**, 119–123 (2014).
57. F. Langer, M. Hohenleutner, C. P. Schmid, C. Poellmann, P. Nagler, T. Korn, C. Schüller, M. S. Sherwin, U. Huttner, J. T. Steiner, S. W. Koch, M. Kira, R. Huber, Lightwave-driven quasiparticle collisions on a subcycle timescale. *Nature* **533**, 225–229 (2016).
58. F. Langer, C. P. Schmid, S. Schlauderer, M. Gmitra, J. Fabian, P. Nagler, C. Schüller, T. Korn, P. G. Hawkins, J. T. Steiner, U. Huttner, S. W. Koch, M. Kira, R. Huber, Lightwave valleytronics in a monolayer of tungsten diselenide. *Nature* **557**, 76–80 (2018).
59. K. Uchida, T. Otobe, T. Mochizuki, C. Kim, M. Yoshita, H. Akiyama, L. N. Pfeiffer, K. W. West, K. Tanaka, H. Hirori, Subcycle optical response caused by a terahertz dressed state with phase-locked wave functions. *Phys. Rev. Lett.* **117**, 277402 (2016).
60. P. G. Zotev, Y. Wang, D. Andres-Penares, T. Severs-Millard, S. Randerson, X. Hu, L. Sortino, C. Louca, M. Brotons-Gisbert, T. Huq, S. Vezzoli, R. Sapienza, T. F. Krauss, B. D. Gerardot, A. I. Tartakovskii, Van der Waals materials for applications in nanophotonics. *Laser Photon. Rev.* **17**, 2200957 (2023).
61. Refractiveindex.info, Refractive index database, https://refractiveindex.info/.
62. N. Piccioli, R. le Toullec, M. Mejatty, M. Balkanski, Refractive index of GaSe between 0.45 μm and 330 μm. *Appl. Optics* **16**, 1236–1238 (1977).

Acknowledgments: We acknowledge Z. Tao and S. Meng for illuminating discussions.
Funding: This work was supported by: National Key Research and Development Program of China (2021YFA1400201) (to T.D. and H.H.), NSFC (no. 12488201) (to N.W. and E.W.), National Key Research and Development Program of China (2022YFA1403500) (to K.L.), National Key Research and Development Program of China (2022YFA1403901) (to N.W.), National Postdoctoral Program for Innovative Talents (BX20200016) (to L.Y.), China Postdoctoral Science Foundation (2021 M700257) (to L.Y.), China Postdoctoral Science Foundation (2022 M710232) (to C.L.), China Postdoctoral Science Foundation (2020 M680177) (to H.H.), and China Postdoctoral Science Foundation (2021 T140022) (to H.H.) **Author contributions:** L.Y., T.D., and N.W. conceived the project. L.Y. performed the nonlinear optical wave mixing measurements. L.Y. measured the wavelength-dependent THG susceptibility. C.L. measured the thickness dependence of THG. C.L. and H.H. performed the nonlinear waveguided wave mixing measurements with help from K.L. and E.W. S.H. and D.W. grew the $MnPSe_3$ and $MnPS_3$ crystals. Q.L., J.Q., and Y.W. prepared the thin films of $MnPSe_3$, WS_3, and GaSe. L.Y., C.L., T.D., and N.W. interpreted the data and wrote this paper, with input from all the authors. **Competing interests:** The authors declare that they have no competing interests. **Data and materials availability:** All data needed to evaluate the conclusions in the paper are present in the paper and/or the Supplementary Materials.

Submitted 21 December 2023
Accepted 28 June 2024
Published 2 August 2024
10.1126/sciadv.adn6216